Materials Horizons

ROYAL SOCIETY OF CHEMISTRY

COMMUNICATION

View Article Online
View Journal | View Issue

Check for updates

Cite this: *Mater. Horiz.*, 2026, 13, 262

Received 3rd August 2025,
Accepted 29th September 2025

DOI: 10.1039/d5mh01476j

rsc.li/materials-horizons

Solvent-triggered off-to-on circular polarization activation *via* scattering modulation in polymer-based chiral photonic particles for encryption and authentication

Fang Zeng,[ab] Honghan Ji,[bc] Zhi-Wang Luo,[b] Jiannan Xiao,[b] Xuefeng Yang,[bc] Jiang Huang,[bc] Qianming Wang *[a] and Pengfei Duan *[bc]

Photonic crystals have attracted significant attention for their structural colors and stimuli-responsive optical properties. However, conventional systems often suffer from undesirable "on-to-off" switching behavior, where structural color fades upon environmental stimulation, limiting their dynamic functionality. To overcome this limitation, we introduce a polymer-based chiral photonic crystal that exhibits an unconventional "off-to-on" switching mechanism governed by scattering modulation. In its dried state, circularly polarized (CP) light is concealed due to strong scattering, rendering the chiral signal optically inactive. Upon solvent infiltration, a reduced refractive index contrast suppresses scattering, activating vivid chiral structural colors. This scattering-driven concealment and reversible activation offer new opportunities for secure optical systems. We demonstrate its application in photonic security labels, where solvent exposure selectively reveals CP light-based patterns that remain hidden under ambient conditions and become fully visible under a polarizer. Furthermore, the inherent variability from particle assembly enables physically unclonable functions for instrument-based authentication, with encoding derived from structural randomness and CP light responses. Together, this system provides a robust, solvent-responsive and polarization-stealth photonic platform for secure information storage and anti-counterfeiting technologies.

New concepts

This work presents a novel class of solvent-responsive chiral photonic crystals (PhCs) featuring an innovative off-to-on switching mechanism for circularly polarized (CP) light reflection and CP luminescence, driven by scattering modulation. Unlike traditional chiral PhCs that rely on internal liquid crystalline reordering for optical modulation, our system employs a rigid, polymerized architecture, eliminating the need for liquid crystal phases and ensuring superior stability and durability. Solvent infiltration reduces the refractive index contrast, suppressing scattering to reveal vivid CP structural color and enhanced CP luminescence. This system enables reversible CP light switching and supports advanced CP luminescence-based applications, such as dynamic optical encryption and secure authentication. These advancements offer new insights into scattering modulation for responsive optical materials, addressing the limitations of traditional chiral PhCs in practical applications.

Introduction

Circularly polarized (CP) light has emerged as a cornerstone of modern optics, distinguished by its unique ability to encode information through its polarization state.[1–4] This phenomenon enables a diverse array of cutting-edge applications, including optical encryption, chiral sensing, three-dimensional displays, and high-density data storage.[5–12] The precise manipulation of light polarization offers significant advantages, enhancing the functionality of photonic devices and enabling innovative approaches to secure information processing and advanced optical systems. In recent years, researchers have developed intelligent, responsive CP light materials capable of dynamically adjusting their optical properties in response to external stimuli such as temperature, solvent exposure, or mechanical stress.[13–15] These advancements aim to achieve tunable, real-time control over CP light, paving the way for next-generation photonic technologies with adaptive and multifunctional capabilities.

Photonic crystals (PhCs) are periodic dielectric structures that can control the propagation of light through their photonic bandgaps (PBGs).[16–18] While conventional achiral PhCs efficiently modulate intensity and wavelength, they lack polarization selectivity, particularly CP light.[19–21] To overcome this limitation, chiral PhCs have been introduced, incorporating helical structures that interact with CP light, enabling light polarization modulation and high dissymmetry factors (*g*-factors) for selective

[a] *School of Chemistry, Guangzhou Key Laboratory of Analytical Chemistry for Biomedicine, South China Normal University, Guangzhou, 510006, P. R. China. E-mail: qmwang@scnu.edu.cn*

[b] *Laboratory of Nanosystem and Hierarchical Fabrication, National Center for Nanoscience and Technology (NCNST), No. 11, ZhongGuanCun BeiYiTiao, Beijing, 100190, P. R. China. E-mail: duanpf@nanoctr.cn*

[c] *University of Chinese Academy of Sciences, No. 19(A) Yuquan Road, Shijingshan District, Beijing, 100049, P. R. China*

reflection, emission, or scattering.[22–25] The commonly used materials for fabricating chiral PhCs are chiral nematic liquid crystals (N*LCs), which self-assemble into helical superstructures with PBGs.[26–29] By adjusting the concentration of chiral dopants, the PBGs of N*LC-based chiral PhCs can be precisely aligned with specific wavelengths, achieving large *g*-factors in reflection (g_{ref}). This approach has shown significant potential, particularly in applications requiring vivid structural colors and polarization selectivity. Recent advances, including notable work by Yu, have demonstrated the potential of polymer microspheres embedded with liquid crystalline phases.[30] Lagerwall, meanwhile, has contributed significantly to the development and understanding of liquid crystal-based microcapsules.[31,32] However, a critical limitation of N*LC-based systems emerges under practical conditions. Immediately after fabrication, these materials exhibit an "on" state, characterized by vivid optimal chiral structural color.[33] Yet, external stimuli—such as thermal fluctuations, solvent infiltration, or mechanical stress—disrupt the helical arrangement, switching the system to an "off" state.[34] This transition results in degradation of the photonic bandgap, loss of polarization selectivity and diminished CP light. Unlike ideal responsive systems that remain "off" until activated, chiral PhCs typically exhibit an inverse "on-to-off" switching behavior—losing color and CP response upon stimulation. This limits their applicability in controlled optical systems and compromises operational stability under real-world conditions. In contrast, our approach enables an unconventional 'off-to-on' response, in which the signals remain hidden until deliberately activated, a switching pathway inherently more secure for encryption applications.

To address these limitations, we propose a polymer-based chiral PhC material enhancing encryption and authentication security *via* polarization stealth and scattering-induced concealment. An emulsion polymerization strategy was employed to fabricate chiral PhC particles, wherein the chiral liquid crystal directed the formation of a helical superstructure within the polymer matrix (Fig. S1a). After polymerization, the chiral liquid crystal template is extracted, resulting in chiral PhC polymer particles characterized by a flattened-spheroid morphology (Fig. 1a).[35] Unlike conventional liquid crystal microspheres or microcapsules, which typically adopt spherical geometries and rely on reconfigurable liquid crystalline interiors, the chiral PhC particles reported here possess a rigid, polymerized chiral architecture with a flattened-spheroid

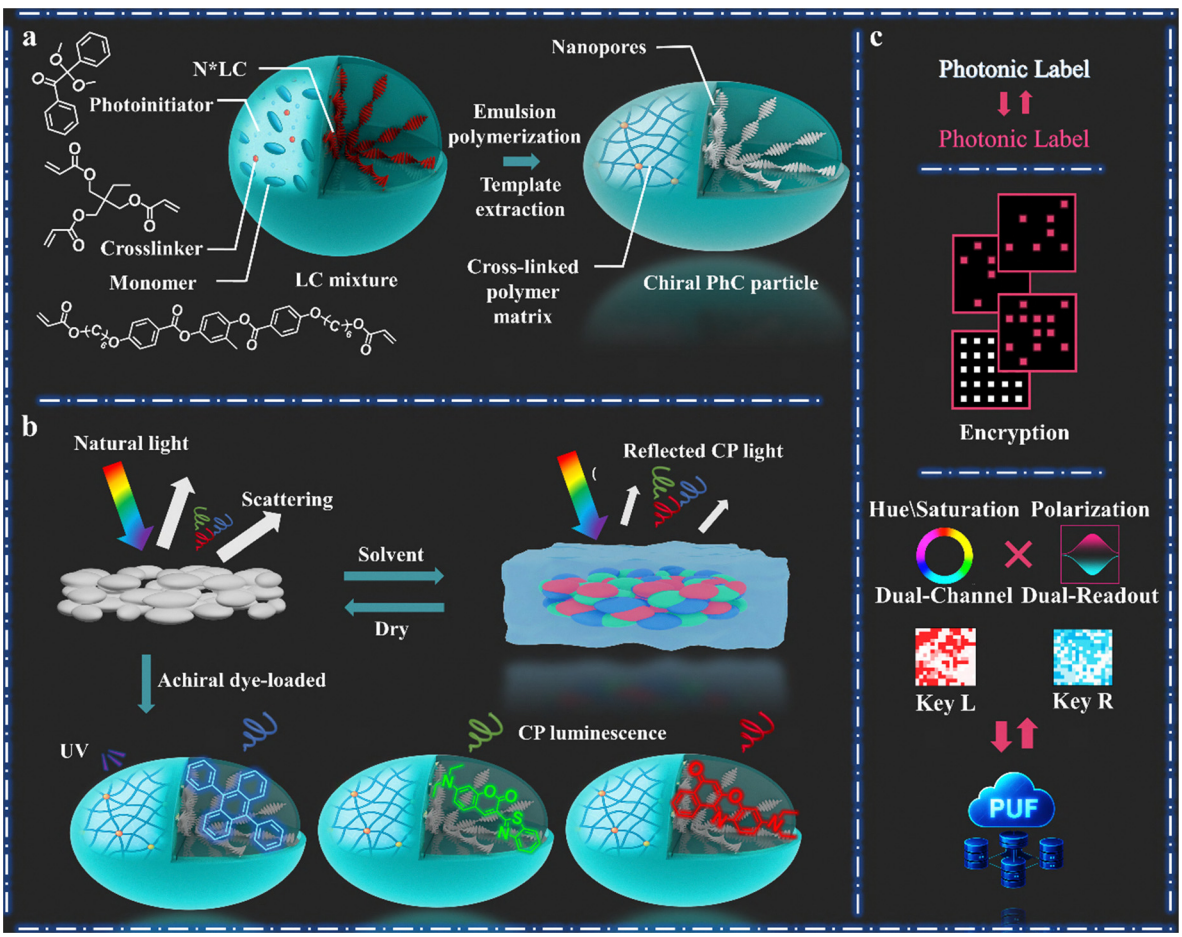

Fig. 1 Scheme illustration of (a) the fabrication process of chiral PhC particles, (b) the "off-to-on" switching mechanism driven by scattering modulation, which can be further extended to dye-loaded systems to achieve CP luminescence and (c) chiral PhC particle applications: photonic label (top), encryption (middle), and physical unclonable function (bottom).

shape.[30,31,36] This structural distinction is critical: LC-based microcapsules achieve optical modulation through internal molecular realignment of fluid mesogens, rendering them highly sensitive to environmental disturbances such as temperature and stress. In contrast, the chiral PhC particles in this work are solid-state systems with a permanently fixed helical superstructure. Their optical behaviour is governed predominantly by scattering modulation rather than dynamic LC reordering. This allows for stable, solvent-triggered switching without the thermotropic limitations common in soft LC systems. In their initial aggregated state, our chiral PhC particles exhibit significant light scattering, effectively concealing their inherent chiral structural color and suppressing circular differential reflection[37] (CDR; circular dichroism signals recorded by the instrument originate from circular differential reflection rather than absorption-based differences; here we defined it as CDR and g_{ref}). In the aggregated state, strong scattering conceals the structural color, yielding a macroscopically white "off" state. Solvent infiltration lowers refractive index contrast, reduces scattering, and reveals vivid chiral color with enhanced CDR, completing the transition to the "on" state. Unlike conventional systems, our chiral PhC particles achieve the desired "off-to-on" response with improved environmental tolerance. We note that minor solvent-induced conformational effects of the polymer framework may also contribute, although the relatively small and reversible spectral shifts observed during repeated solvent cycling (Fig. S11) indicate that such contributions are limited and secondary to refractive index matching. This solvent-triggered, scattering-driven mechanism not only resolves the constraints of prior systems, but also establishes a versatile platform for advanced optical applications. Based on its many advantages, we implement its functional application. CP light enables encryption *via* its concealed polarization, detectable only with specialized tools, ensuring inherent security. Our scattering-driven mechanism enhances this by masking CP light with strong scattering, unveiling it only upon solvent stimulus.

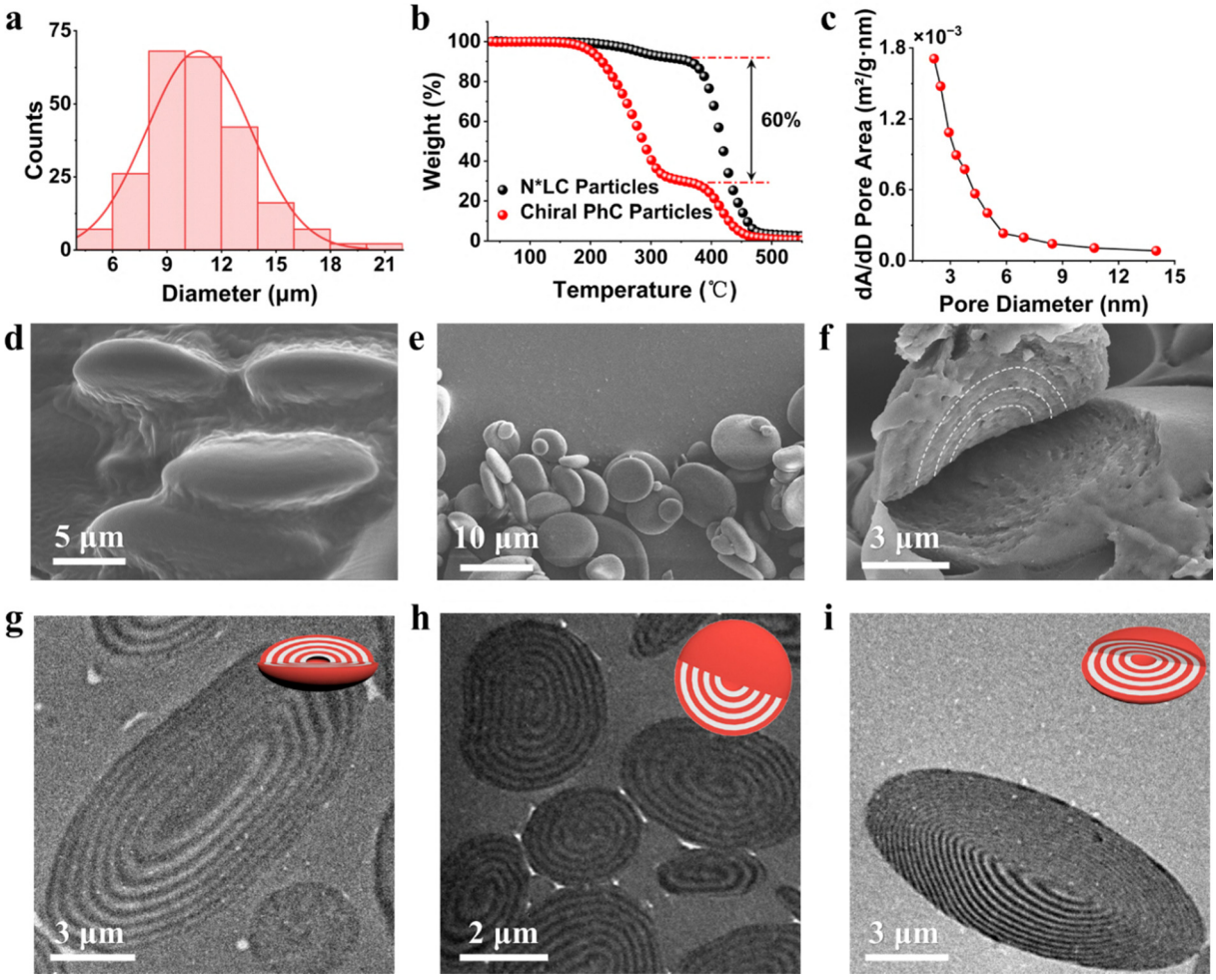

Fig. 2 Structural and morphological characterization of the chiral PhC particles. (a) Size distribution of the chiral PhC particles (average ~10 μm). (b) TGA curves showing ~60 wt% loss due to the removal of unpolymerized components. (c) Pore size distributions of the chiral PhC particles, S5011/HTG135200 = 2.2 wt%. (d)–(f) SEM images: (d) ellipsoidal N*LC polymer particles in dry PVA; (e) morphology of the chiral PhC particles; (f) internal concentric ellipsoidal structure revealed by fracture, highlighted with white dashed lines. (g)–(i) TEM images of the chiral PhC particles sliced along different orientations, revealing periodic internal structures (insets show slicing directions).

This dual approach—polarization stealth plus scattering-induced concealment—greatly bolsters optical authentication and encryption security (Fig. 1b and c). In addition, the oil-in-water emulsion polymerization strategy employed here is an established, scalable process that enables mass production of monodisperse chiral PhC microparticles. Together with the robust solid-state polymer framework and the reversible solvent-triggered activation, this approach provides a practical and durable pathway toward encryption applications.

Results and discussion

Fabrication and characterization of chiral PhC particles

Chiral PhC particles were prepared using liquid crystals (LCs) comprising a mixture containing N*LC, chiral dopant, monomers, photoinitiator and a crosslinker (Table S1). The internal nanoporous architecture retains the helicoidal arrangement of the N*LC, with handedness determined by the chiral dopant.[35] The mixture was emulsified in polyvinyl alcohol (PVA) aqueous solution to form a stable oil-in-water (O/W) emulsion. A 10 wt% PVA solution was chosen as optimal under our experimental conditions, since lower concentrations (<7 wt%) failed to yield stable emulsions, whereas higher concentrations led to smaller particles with reduced thickness. Upon drying, droplet shrinkage stress induced a shape transformation from spherical to ellipsoidal shapes.[38] UV irradiation subsequently polymerized the aligned liquid crystal monomers, locking the chiral photonic structure (Fig. S1). After removal of the matrix and residual components, free-standing particles with an average diameter of ~10 μm were obtained (Fig. 2a).

Thermogravimetric analysis (TGA) here demonstrates a substantial weight loss of approximately 60 wt% from the LC unwashed N*LC polymer particles compared to the final purified chiral PhC particles (Fig. 2b), closely matching the theoretical value of 61.9 wt%. This confirms the efficient removal of non-reactive liquid crystal components. Meanwhile, X-ray diffraction (XRD) exhibits similar diffraction patterns among

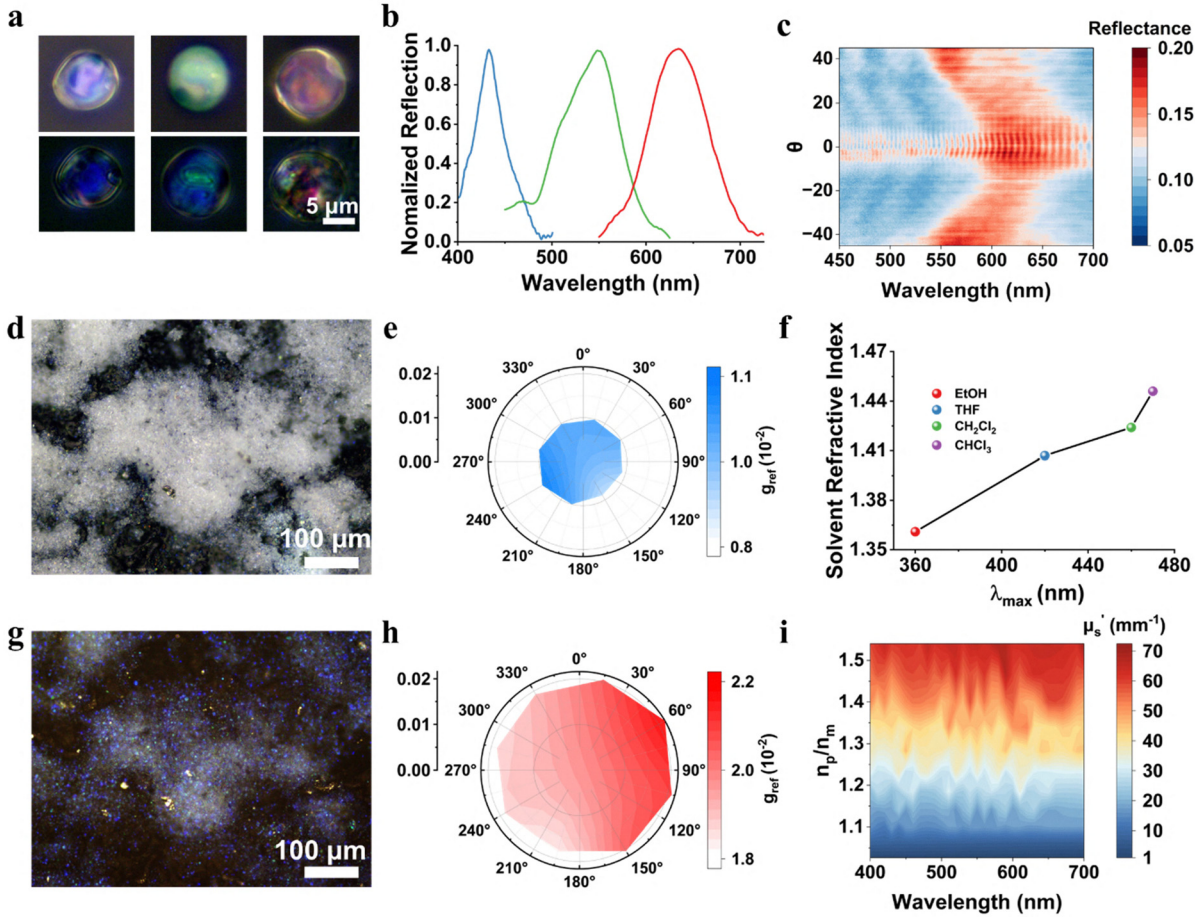

Fig. 3 Photophysical characterization of chiral PhC particles. (a) Micro-reflectance (top) and POM (bottom) images of chiral PhC particles with different photonic bandgaps. (b) Reflectance spectra of individual chiral PhC particle samples. (c) Angle-resolved micro-reflectance spectroscopy (ARMS) of chiral PhC particles. (d) Micro-reflectance images of chiral PhC particles in the dry state. (e) g_{ref} values of chiral PhC particles in the dry state measured at different angles. (f) CDR peak positions of chiral PhC particle samples with solvents of varying refractive indices. (g) Micro-reflectance images of chiral PhC particles in water. (h) g_{ref} values of chiral PhC particles in water at different angles. (i) Calculated reduced scattering coefficients (μ_s') *versus* refractive index ratio (n_p/n_m) from 400 to 700 nm.

N*LC, N*LC polymer particles, and chiral PhC particles, suggesting that the chiral nanostructure framework of the N*LC is effectively imprinted into the polymerized N*LC particles and further retained in the chiral PhC particles (Fig. S2). The analysis reveals that the resulting nanoporous architecture, characterized by N_2 adsorption–desorption isotherms, consists of pores below 10 nm in diameter, with an average pore size of ~7 nm (Fig. 2c). The scanning electron microscopy (SEM) image reveals the internal periodic architecture of the flattened-spheroid photonic crystal particles, displaying well-defined concentric elliptical layers radiating from the core to the outer surface, which ensures long-range periodicity required for the formation of PBGs (Fig. 2d–f). Transmission electron microscopy (TEM) further confirms this periodic structure, displaying varied elliptical and layered patterns depending on slicing orientation (Fig. 2g–i).

Photophysical properties of the chiral PhC particles

Under optical microscopy, separated chiral PhC particles exhibit vivid structural color originating from their chiral PBGs (Fig. 3a and b). The chirality of the chiral PhC particles is determined by the choice of chiral dopant, while the reflection wavelength can be tuned by adjusting the ratio of LCs to chiral dopant. Upon removal of the liquid crystal component, CDR spectroscopy revealed a pronounced blue shift[39] (Fig. S5), indicating a reduction in the helical pitch of the chiral photonic structure. Polarized optical microscopy (POM) provided additional evidence of this transformation, as the characteristic Maltese cross pattern disappeared and the originally spherical microparticles adopted a more flattened morphology (Fig. S5). Compared to previously reported spherical LCs, chiral PhC particles exhibit a significantly broader reflection range due to their flattened-spheroid geometry, which enhances the visibility of their photonic response, leading to angle-dependent reflection, where the reflected wavelength shifts systematically with variations in the viewing or illumination angle (Fig. 3a, c). This behavior is characteristic of planar photonic crystal films and can be described by Bragg's law:[37]

$$\lambda = 2n_{\text{eff}}P\cos\theta$$

where λ is the reflected wavelength, n_{eff} is the effective refractive index, P represents the helical pitch, and θ is the incident angle.

An intriguing phenomenon arises when observing chiral PhC particles from a macroscopic perspective. In their dry state, chiral PhC particles appear as a white, powder-like material, with its inherent structural color imperceptible (Fig. 3d). Correspondingly, their optical activity remains weak, with g_{ref} detectable around 1.1×10^{-2} (Fig. 3e). However, upon water (n = 1.33) incorporation, chiral PhC particles undergo a transformation—and its vivid chiral structural color emerges and becomes clearly visible (Fig. 3g), accompanied by a significant increase in g_{ref} (Fig. 3h). This behavior appears counter-intuitive to conventional expectations for photonic crystals, where solvent infiltration typically weakens the structural color by reducing the refractive index contrast.[40] In colloidal PhCs, for instance, solvent incorporation lowers reflection efficiency, as described by Fresnel's equations:

$$R = \left(\frac{n_1 - n_2}{n_1 + n_2}\right)^2$$

where R represents the reflectance, n_1 is the refractive index of the material, and n_2 is the refractive index of the surrounding environment.

When a solvent with a higher refractive index infiltrates the photonic crystal structure, it replaces air (n = 1), leading to a decrease in the refractive index contrast between the material and its environment. This results in reduced reflection and a fading of structural color, indicating a weakened light modulation capability. In chiral photonic crystals, this weakening corresponds to a diminished selective circularly polarized reflection, resulting in a reduction in CDR.[41]

Mechanism of solvent-triggered "off-to-on" switching

Upon closer inspection, we find that the observed phenomenon remains aligned with theoretical predictions by systematically increasing the refractive index of the solvent used and analyzing chiral PhC particles under a microscope. When THF (n = 1.46) is introduced, chiral PhC particles' structural color becomes entirely imperceptible, and its transparency increases further as the environmental refractive index rises, which is in accordance with Fresnel's equations, as the reduced refractive index contrast leads to decreased reflection (Fig. S7). Simultaneously, this increase in environmental refractive index also induces a redshift of the CDR wavelength, consistent with Bragg's law (Fig. 3f). The additional scattering effects brought by the chiral PhC particles contribute to the seemingly contradictory phenomenon we observe. To investigate this effect, Mie theory was applied to model their light-scattering behavior in different media.[42] The scattering anisotropy factor g and scattering coefficient μ_s were calculated using classical Mie formulations, incorporating Bessel and Hankel functions to describe multipole expansions of the scattered fields.

$$g = \frac{4}{k^2\mu_s}\sum_{n=1}^{\infty}\left[\frac{n(n+2)}{n+1}\text{Re}(a_n a_{n+1}^* + b_n b_{n+1}^*) + \frac{2n+1}{n(n+1)}\text{Re}(a_n b_n^*)\right]$$

$$\mu_s = \frac{2\pi}{k^2}\sum_{n=1}^{\infty}(2n+1)\left(|a_n|^2 + |b_n|^2\right)$$

With appropriate simplifications, we investigated the influence of the refractive index contrast on the reduced scattering coefficient μ_s', which quantifies the scattering. As shown in Fig. 3i, μ_s' increases with the refractive index ratio n_p/n_m. This trend aligns well with Mie theory, where a higher refractive index contrast between the particle and the surrounding medium leads to stronger scattering due to increased phase discontinuity at the particle–medium interface. This effect is particularly evident in the aggregated state of chiral PhC particles. While well-dispersed particles display vivid structural color under a microscope. The ellipsoidal morphology of the powder-form chiral photonic crystal (PhC) particles further

complicates their optical behavior. The random orientation and aggregation inherent to this shape enhance anisotropic scattering, as evidenced by the increased reduced scattering coefficient μ_s' with higher refractive index contrast (Fig. 3i). This effect distinguishes our work from studies on uniform spherical particles, where controlled photonic properties are achieved,[43] highlighting the novel role of ellipsoidal geometry in scattering-driven concealment. The powder-like nature of these ellipsoidal particles, characterized by random aggregation, poses challenges for orientation control, a potential avenue for future exploration. Nonetheless, this aggregation amplifies non-polarized scattering, effectively masking the structural coloration and reducing circularly polarized reflection and CDR signals (Fig. 4a–c). Upon solvent infiltration, the refractive index contrast between the chiral PhC particles and the surrounding medium decreases, thereby weakening the scattering intensity. This reduction in scattering allows the tuned chiral-polarized reflection to emerge more distinctly, manifesting as the appearance of structural color. Simultaneously, the suppression of non-polarized scattering enhances the CDR signals, making them more pronounced (Fig. 4a–c). This phenomenon underscores the crucial role of the scattering environment in modulating the optical response of the chiral PhC particle and provides a novel approach to dynamically control its chiroptical properties through solvent-induced refractive index tuning.

Building upon our previous work,[35] we leverage the intrinsic nanoporous structure of chiral PhC particles to create a physical chiral environment that promotes strong host–guest interactions with achiral dyes, thereby imparting circularly polarized luminescence to these molecules. To further explore chiral PhC particle's CP luminescence properties, we selected three representative dyes: coumarin 6 (C6), a planar dye exhibiting aggregation-caused quenching (ACQ) due to π–π stacking in its aggregated state; 9,10-diphenylanthracene (DPA), another ACQ dye with high fluorescence efficiency in dilute solutions but prone to excimer formation and quenching upon aggregation; and Nile Red (NR), an ACQ dye highly sensitive to environmental polarity, undergoing fluorescence quenching upon aggregation in aqueous or polar media. These dyes were incorporated into chiral PhC particles with tailored photonic bandgaps by immersion in methanol solutions ([dye] = 0.1 mg mL^{-1})

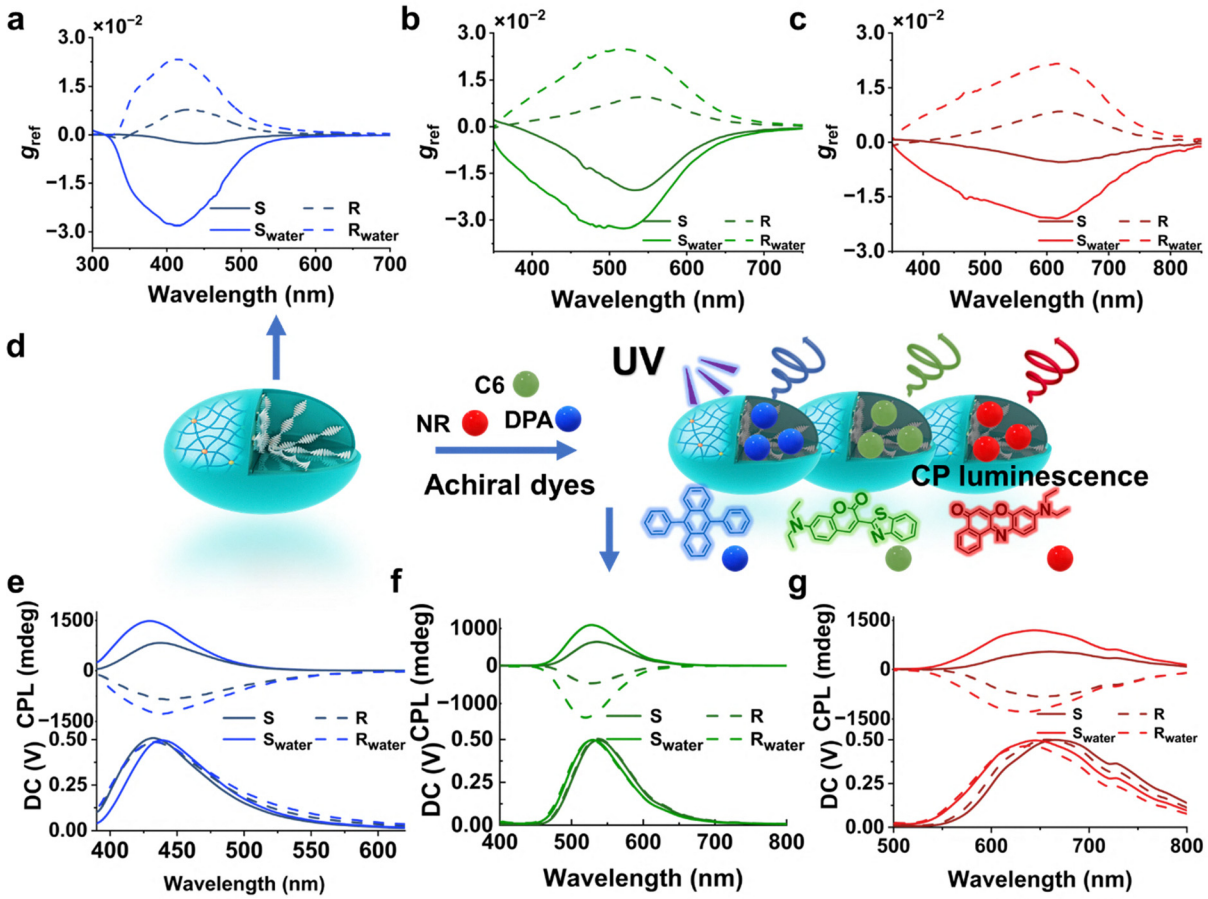

Fig. 4 Chiral optical responses of chiral PhC particles. (a)–(c) g_{ref} spectra of the chiral PhC particles with photonic bandgaps in the blue, green, and red regions, respectively, each displaying chiral PhC particles under dry conditions and with enhanced CDR in an aqueous environment. (d) Schematic of dye loading into the chiral PhC particles and generation of CP luminescence upon UV excitation. Insets show the chemical structures of the corresponding dyes: DPA (blue), C6 (green), and NR (red). (e)–(g) CP luminescence spectra of the chiral PhC particles loaded with dyes, measured under the same conditions as in (a)–(c). Excitation wavelengths: 360 nm for (d) and 365 nm for (e) and (f). Detailed molecular information is provided in Table S1.

for six hours, followed by centrifugation to yield dye-loaded chiral PhC particle materials. As expected, the incorporation of these dyes into the chiral PhC particles resulted in distinct CP luminescence, demonstrating excellent luminescence dissymmetry and solvent responsiveness. The structural confinement and chiral environment provided by the chiral PhC particles effectively lead to the emergence of CP luminescence activity. Notably, all dye-loaded chiral PhC particle composites exhibited a pronounced increase in $|g_{lum}|$, exceeding 0.2 upon exposure to water, indicating remarkable solvent-induced CP luminescence enhancement (Fig. 4e–g). The observed CP luminescence enhancement upon water interaction is attributed to

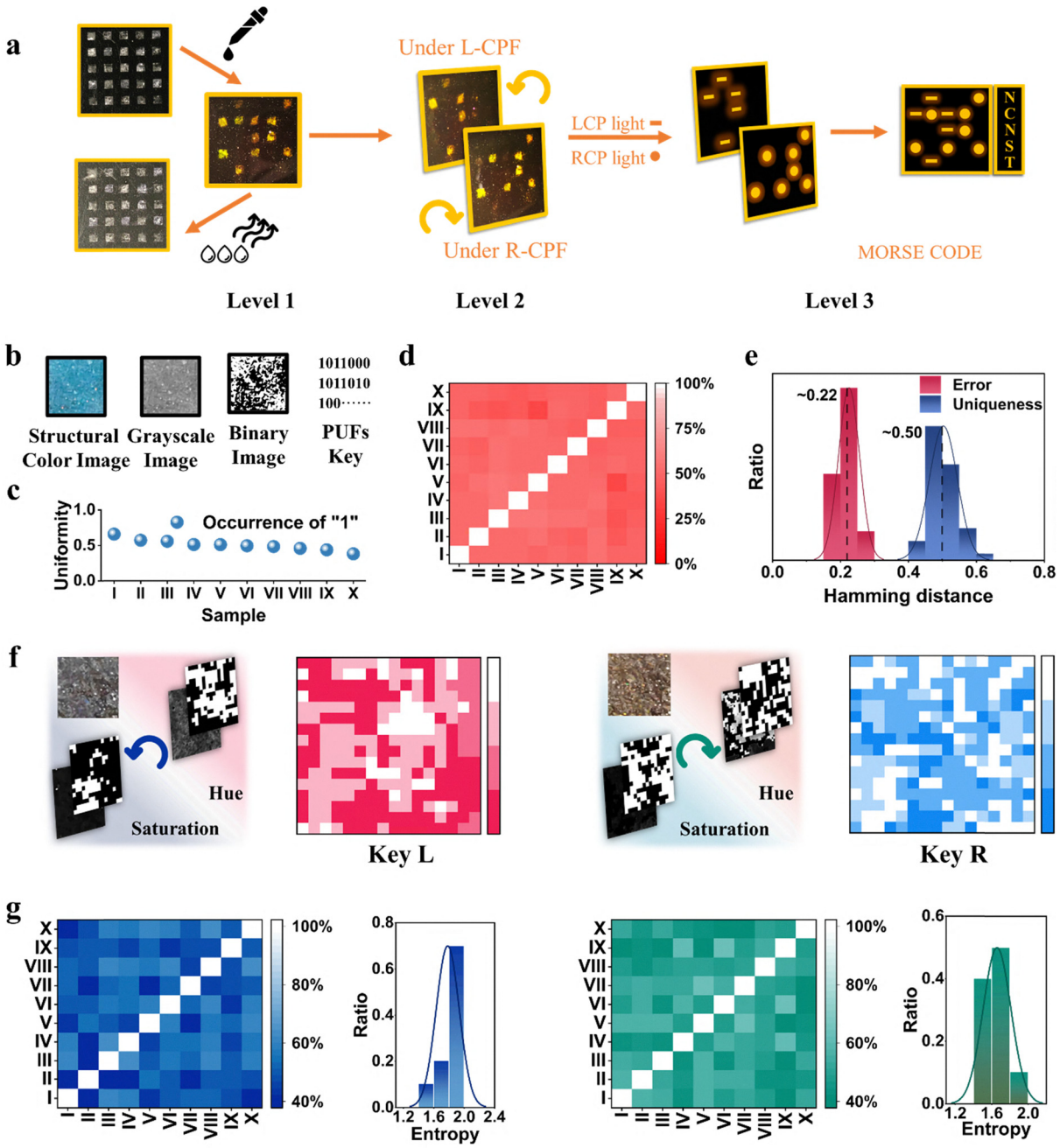

Fig. 5 Multilevel information encryption and PUFs of chiral PhC particles. (a) Three-level encryption in a 5 × 5 array: level 1, concealed by strong scattering; level 2, chiral structural colors revealed after solvent exposure; level 3, left- and right-handed CPF decoding to generate Morse code ("NCNST"). (b) Generation of PUF keys from structural color, grayscale, and binarized images of chiral PhC particle patterns. (c) Randomness analysis showing near-ideal distribution of binary values. (d) Reproducibility of readout from repeated measurements of the same sample. (e) Inter-sample uniqueness and intra-sample bit error rate derived from Hamming distance analysis. (f) Dual-channel quaternary encoding: hue and saturation channels under left and right CPF yield distinct binary maps, which are combined into quaternary keys (0–3) for each pixel. (g) Reproducibility, uniqueness, and entropy of keys L and R, demonstrating high randomness and robustness of the quaternary PUF scheme.

a reduction in the scattering coefficient of the chiral PhC particles. Water infiltration decreases the refractive index contrast between the polymer and its surroundings, suppressing scattering and enhancing the transmission of chiral optical signals. Furthermore, the nanoporous structure of the chiral PhC particle prevents the ACQ of C6, DPA, and NR by inhibiting their aggregation, thereby preserving their fluorescence while inducing CP luminescence. The purity of the CP luminescence was confirmed by angle-resolved CPL measurements, where both intensity and handedness remained invariant upon sample rotation (Fig. S9c), further validating the circular polarization nature. This dual functionality—mitigating ACQ and amplifying dissymmetry—highlights chiral PhC particle's potential as a tunable platform for advanced photonic applications.

Applications of the chiral PhC particles

The chiral polarization of CP light-active materials makes them ideal for encryption and authentication. We demonstrated this by printing ''NCNST'' using chiral PhC particles with distinct PBGs (Fig. S11a). Solvent exposure triggered a concealed-to-revealed transition, showing vivid chiral colors under a CP filter for visual authentication. The tag remained reversible and stable over repeated cycles (Fig. S11b), highlighting its potential as a robust, reusable anti-counterfeiting platform. Building on this functionality, we developed a multilevel encryption strategy integrating CP light with solvent responsiveness to achieve high security, concealment, and reversibility. A 5×5 array was constructed using three types of microparticles—achiral (no PBG), left-handed, and right-handed chiral PhC particles (Fig. 5a). Initially, strong scattering renders the entire array uniformly white, masking all optical features. Upon solvent infiltration, reduced scattering reveals distinct responses: achiral squares become transparent, while chiral ones exhibit vivid yellow structural color, selectively visible through CPF. Viewed through a left or right circular CPF, only the corresponding handed particles display Morse code dots and dashes, respectively, revealing the message ''NCNST.'' Solvent evaporation restores scattering, returning the system to its concealed, opaque state. This reversible cycle enhances security: scattering hides signals, and solvent and CPF reveal them, and evaporation re-masks them. This solvent-triggered, self-resetting system enables robust chiral encryption for optical security.

The inherent size variability of chiral PhC particles imparts unique, irreproducible patterns when assembled, making them ideal candidates for optical physical unclonable function (PUF) platforms—security systems that leverage physical randomness to generate unpredictable, non-replicable identifiers.[44] The solvent-responsive structural color and concealed CP light further enhance resistance to counterfeiting. Unlike conventional excitation-based optical PUFs that suffer from photobleaching (*e.g.*, those using dyes or luminescent materials), our system operates *via* reflection, ensuring long-term durability and stability. This reflection-based mechanism, combined with dynamic optical responsiveness to environmental stimuli, offers a robust and tamper-resistant solution for high-security applications. Following the multilevel encryption demonstrated in Fig. 5a, we next standardized structural color images from individual samples into uniform 512×512 grayscale images. By comparing pixel brightness across samples, a threshold was applied to assign binary values: pixels above the threshold were encoded as ''1,'' and those below as ''0.'' This process generated n-bit binary keys, enabling quantitative analysis of pattern uniqueness and stability (Fig. 5b). Randomness was quantified by calculating the ratio of ''1'' values to the total key length. This ratio directly reflects whether the thresholding process generates an unbiased distribution of ''0'' and ''1,'' and thus whether the chosen threshold is suitable. The calculation is expressed as:

$$F_{\text{randomness}} = \frac{1}{n}\sum_{i=1}^{n} N_i$$

Here, N_i and n denote the i-th binary key and key length, respectively. As shown in Fig. 5c, the probability of a single key being ''0'' or ''1'' is approximately 0.5, close to the ideal value of 0.5, confirming the data's randomness. To assess reproducibility, multiple images of the same sample were collected and analyzed under identical conditions. The stability of the PUF readout was quantified using the Hamming distance, which measures the bit error rate between repeated keys of the same sample:

$$R_{\text{redout reproducibility}} = \frac{1}{T}\sum_{i=1}^{T}\frac{n - D_{\text{H}}(N_i, N_{i,t})}{n}$$

Here, N_i and $N_{i,t}$ denote the i-th key of n-length from T repeated measurements of the mapping images. Fig. 5d shows that the statistical consistency between repeated measurements confirms the high reproducibility of PUF readouts from the same sample. While reproducibility is high within the same sample, variability introduced during sample preparation ensures that different samples remain inherently random. To evaluate this uniqueness, the Hamming distance (DH) was calculated between binary keys from different samples. This metric quantifies the probability that two keys differ at corresponding pixel positions, and is defined as:

$$H_{\text{uniqueness}} = \frac{2}{C(C-1)}\sum_{i=1}^{C(C-1)}\frac{D_{\text{H}}(N_i, N_{i,c})}{n}$$

Here, N_i and $N_{i,c}$ denote the i-th binary key of different n-length keys, with C total n-length keys, respectively. The error, quantified as H_{error}, measures discrepancies during image capture and encoding. As shown in Fig. 5e, the error probability for repeated measurements of the same sample was approximately 0.22, notably lower than the uniqueness between different samples (~ 0.5).

To enhance the security and information density of the optical PUF platform, we developed a dual-channel quaternary encoding strategy that leverages both polarization-dependent readout and structural color characteristics of chiral PhC particles. Specifically, dual readout under left- and right-handed CPF yields distinct hue-saturation (HS) responses,

enabling two independent keys—key L and key R. Each key is generated through thresholding the hue and saturation channels of the structural color images to produce binary values (“0” or “1”) per channel. These are then combined into a quaternary code (“00,” “01,” “10,” or “11,” corresponding to “0”–“3”) for each pixel, effectively doubling the encoding capacity compared to traditional binary schemes (Fig. 5f). This polarization-resolved, color-based dual-channel approach significantly enhances entropy, increases information density, and improves resistance to counterfeiting, establishing a robust and high-capacity optical PUF system. They also display good readout reproducibility (Fig. 5f), inter-sample uniqueness, intra-sample bit error rate (Fig. S12) and randomness. The average entropy is measured by quantifying the uncertainty in the distribution of quaternary values (0 to 3) in the response matrices. Higher entropy (ideally 2) indicates greater randomness, computed as:

$$\text{Average entropy} = \frac{1}{S}\sum_{i=1}^{S} H_i$$

$$H_i = -\sum_{v=0}^{3} p(x)\log_2(p(x))$$

where H_i is the entropy of the i-th PUF instance, $p(x)$ is the probability of value x across all response matrices of the instance, and S is the number of PUF instances. The entropy values, typically close to the ideal of 2 bits, confirm the high randomness of the quaternary PUF responses (Fig. 5g).

Conclusions

In this study, we embedded the helical order of chiral liquid crystals into a cross-linked polymer matrix to construct flattened-spheroid chiral PhC particles that exhibit solvent-triggered, scattering-mediated “off-to-on” switching of CP light. Unlike conventional systems or liquid crystal microspheres that display vivid but environmentally vulnerable “on”-state structural colors, our particles remain optically inactive in the dry state due to strong scattering, and only reveal vivid chiral colors and CP signals upon solvent infiltration. This switching arises from reduced refractive index contrast, enabling dynamic CP light modulation and reversible optical concealment. In contrast to the softness and instability of LC-based microcapsules, our polymeric particles are structurally robust, solvent-responsive, and inherently secure, offering a durable, programmable platform for CP light-based encryption and physically unclonable function PUF authentication.

Author contributions

P. D. conceived the idea and supervised the project. F. Z. and P. D. designed the experiments. F. Z. designed, synthesized and characterized the materials. F. Z. and J. H. carried out the theoretical calculations. P. D., H. J., Q. W., J. X. and F. Z. wrote and revised the manuscript. All authors analysed and discussed the results and have given approval for the final version of the manuscript.

Conflicts of interest

There is no conflict of interest to report.

Data availability

All data supporting this study, including detailed methods and experimental details, and photophysical property studies, are available in the manuscript, and supplementary information (SI). Supplementary information: experimental details, raw materials, calculation methods, refractive index data, SEM images, pore size distributions, ARMS spectra, bright-field, POM, and fluorescence microscopy images for analysis, and photoluminescence and absorption spectra. See DOI: **https://doi.org/10.1039/d5mh01476j**.

All data are available upon request.

Acknowledgements

This work was supported by the National Key Basic R&D Research Program of Ministry of Science and Technology of the People’s Republic of China (2021YFA1200303); the National Natural Science Foundation of China (52173159 and 92256304). Q. M. was grateful to Key-Area Research and Development Program of Guangdong Province (No. 2024B1111100001). We acknowledge Dr Le Zhao from the Nanofabrication Laboratory at NCNST for assistance with refractive index measurements.

Notes and references

1 X. S. Du, X. N. Han, Y. Han and C. F. Chen, *Chem. Commun.*, 2022, **59**, 227–230.
2 R. Rodriguez, C. Naranjo, A. Kumar, P. Matozzo, T. K. Das, Q. Zhu, N. Vanthuyne, R. Gomez, R. Naaman, L. Sanchez and J. Crassous, *J. Am. Chem. Soc.*, 2022, **144**, 7709–7719.
3 F. Song, Y. Cheng, Q. Liu, Z. Qiu, J. W. Y. Lam, L. Lin, F. Yang and B. Z. Tang, *Mater. Chem. Front.*, 2019, **3**, 1768–1778.
4 K. K. Tan, W. C. Guo, W. L. Zhao, M. Li and C. F. Chen, *Angew. Chem. Int. Ed.*, 2024, **63**, e202412283.
5 K. Dhbaibi, L. Abella, S. Meunier-Della-Gatta, T. Roisnel, N. Vanthuyne, B. Jamoussi, G. Pieters, B. Racine, E. Quesnel, J. Autschbach, J. Crassous and L. Favereau, *Chem. Sci.*, 2021, **12**, 5522–5533.
6 D. Han, J. Wang, T. Zheng, L. Peng and T. Jiao, *Cell Rep. Phys. Sci.*, 2023, **4**, 101523.
7 T. Huang, L. Yuan, X. Lu, Y. Qu, C. Qu, Y. Xu, Y. X. Zheng and Y. Wang, *Chem. Sci.*, 2024, **15**, 15170–15177.
8 J. Q. Liang, J. J. Hu, Z. Z. Huo, Z. P. Yan, L. Yuan, X. S. Zhong, Y. Wei, S. Q. Song, Q. M. Liu, Y. Song and Y. X. Zheng, *Chem. – Asian J.*, 2024, **19**, e202400664.
9 S. Lin, Y. Tang, W. Kang, H. K. Bisoyi, J. Guo and Q. Li, *Nat. Commun.*, 2023, **14**, 3005.
10 X. Li, L. Huang, G. Baryshnikov, A. Ali, P. Dai, Z. Yang, Y. Sun, C. Dai, Z. Guo, Q. Zhao, F. Zhang and L. Zhu, *Adv. Mater.*, 2025, e2500236, DOI: **10.1002/adma.202500236**.

11 R. Liu, J. Wei, J. Hao and Z. Yang, *ACS Nano*, 2025, **19**, 20194–20204.
12 X. Mo, G. Chen, Y. Li, B. Xiao, X. Chen, X. Yin and C. Yang, *Chem. Sci.*, 2024, **15**, 17663–17670.
13 K. Fu and G. Liu, *ACS Nano*, 2024, **18**, 2279–2289.
14 J. Liu, J. J. Wu, J. Wei, Z. J. Huang, X. Y. Zhou, J. Y. Bao, R. C. Lan, Y. Ma, B. X. Li, H. Yang, Y. Q. Lu and Q. Zhao, *Angew. Chem. Int. Ed.*, 2024, **63**, e202319536.
15 C. Zhang, Z. S. Li, X. Y. Dong, Y. Y. Niu and S. Q. Zang, *Adv. Mater.*, 2022, **34**, e2109496.
16 X. Yang, J. Lv, J. Zhang, T. Shen, T. Xing, F. Qi, S. Ma, X. Gao, W. Zhang and Z. Tang, *Angew. Chem. Int. Ed.*, 2022, **61**, e202201674.
17 Y. He, S. Lin, J. Guo and Q. Li, *Aggregate*, 2021, **2**, e141.
18 Q. Guo, M. Zhang, Z. Tong, S. Zhao, Y. Zhou, Y. Wang, S. Jin, J. Zhang, H.-B. Yao, M. Zhu and T. Zhuang, *J. Am. Chem. Soc.*, 2023, **145**, 4246–4253.
19 F. Furlan, J. M. Moreno-Naranjo, N. Gasparini, S. Feldmann, J. Wade and M. J. Fuchter, *Nat. Photonics*, 2024, **18**, 658–668.
20 P. Gayathri, S. Q. Qiu and Z. Q. Yu, *Mater. Horiz.*, 2025, **12**, 5627–5653.
21 Q. Qin and Y. Xu, *Adv. Sci.*, 2024, **11**, e2404761.
22 Y. Liu and P. Xing, *Adv. Mater.*, 2023, **35**, 2300968.
23 J. J. Baumberg, O. L. Pursiainen and P. Spahn, *Phys. Rev. B: Condens. Matter Mater. Phys.*, 2009, **80**, 201103(R).
24 S. Bao, S. Li, Z. Tang, Y. Wan, G. Zhou, Z. Yang, D. Sun, D. Ye and L. Zhu, *J. Mater. Chem. C*, 2025, **13**, 9453–9464.
25 Y. Chen, Z. Li, Y. Guan, J. Huang, J. Li, J. Qi, M. Wu, H. Li and H. L. Xie, *Macromol. Chem. Phys.*, 2025, 2500084, DOI: **10.1002/macp.202500084**.
26 B. Chu, F. Song, P. Wang, Y. Cheng and Z. Geng, *ACS Appl. Mater. Interfaces*, 2024, **16**, 26604–26612.
27 J. Lv, X. Yang and Z. Tang, *Adv. Mater.*, 2023, **35**, e2209539.
28 Y. Wu, M. Li, Z. G. Zheng, Z. Q. Yu and W. H. Zhu, *J. Am. Chem. Soc.*, 2023, **145**, 12951–12966.
29 Z. Zhou, X. Cheng, Z. Tang, Y. Wang, Z. He and W. Zhang, *Chem. Commun.*, 2025, **61**, 3880–3883.
30 M. Zhang, Q. Guo, Z. Li, Y. Zhou, S. Zhao, Z. Tong, Y. Wang, G. Li, S. Jin, M. Zhu, T. Zhuang and S.-H. Yu, *Sci. Adv.*, 2023, **9**, eadi9944.
31 X. Ma, Y. Han, Y.-S. Zhang, Y. Geng, A. Majumdar and J. P. F. Lagerwall, *Nat. Commun.*, 2024, **15**, 1404.
32 A. Sharma, R. Kizhakidathazhath and J. P. F. Lagerwall, *Soft Matter*, 2023, **19**, 2637–2645.
33 L. Wen, P. Yang, S. Mo, D. Wang, N. Sheng, X. Xu, H. Zhang, H. Lu and G. Zou, *Chem. Eng. J.*, 2025, **505**, 159821.
34 Y. Choi, D. Choi, J.-K. Choi, K.-S. Oh, E. Cho, J.-H. Im, D. P. Singh and Y.-K. Kim, *ACS Appl. Opt. Mater.*, 2023, **1**, 1879–1897.
35 Y. Shi, J. Han, C. Li, T. Zhao, X. Jin and P. Duan, *Nat. Commun.*, 2023, **14**, 6123.
36 S. S. Lee, H. J. Seo, Y. H. Kim and S. H. Kim, *Adv. Mater.*, 2017, **29**, 1606894.
37 D. J. Mulder, A. P. H. J. Schenning and C. W. M. Bastiaansen, *J. Mater. Chem. C*, 2014, **2**, 6695–6705.
38 P. A. Kralchevsky and N. D. Denkov, *Curr. Opin. Colloid Interface Sci.*, 2001, **6**, 383–401.
39 A. K. Rella, S. Subedi, L. G. Trung, V. Kumar, S. Kim and S. W. Kang, *Small*, 2023, **19**, 2300309.
40 J. Ge and Y. Yin, *Angew. Chem. Int. Ed.*, 2011, **50**, 1492–1522.
41 K. E. Shopsowitz, H. Qi, W. Y. Hamad and M. J. Maclachlan, *Nature*, 2010, **468**, 422–425.
42 H. W. L. V. Wang, in *Biomedical Optics: Principles and Imaging*, John Wiley & Sons, Inc., New Jersey, 2009, p. 17, DOI: **10.1002/9780470177013.ch2**.
43 H. Agha, Y.-S. Zhang, Y. Geng and J. P. F. Lagerwall, *Adv. Photonics Res.*, 2023, **4**, 2200363.
44 J. Huang, X. Jin, X. Yang, T. Zhao, H. Xie and P. Duan, *ACS Nano*, 2024, **18**, 15888–15897.